International Journal of Mechanical System Dynamics

WILEY

IJMSD International Journal of Mechanical System Dynamics Open Access

RESEARCH ARTICLE OPEN ACCESS

A Computational Framework for Predicting Vibrations in the Front-Loading Washing Machine Using Component-Level Experiments and Mathematical Modeling

Dae-Guen Lim[1] | Seok-Chan Kim[2] | Min-Ho Pak[2]

[1]Department of Mechanical Engineering, KAIST, Daejeon, Republic of Korea | [2]H&A VPD SHIL, LG Electronics, Changwon, Republic of Korea

Correspondence: Min-Ho Pak (minho.pak@lge.com)

Received: 18 November 2024 | **Revised:** 23 January 2025 | **Accepted:** 22 February 2025

Funding: The research reported in this paper has been supported by LG Electronics, Republic of Korea.

Keywords: front-loading washing machine | mathematical modeling | multibody dynamics

ABSTRACT

This study proposes a computational framework for developing a multibody dynamics (MBD) model to accurately predict the vibration behavior of front-loading washing machines. The framework integrates component-level experiments and mathematical modeling to characterize the dynamic behavior of key components, including the free-stroke damper, connecting bushing, and gasket, which significantly influence the machine's vibration. Simplified, yet precise, mathematical models were developed and validated against experimental data to represent these components' dynamic characteristics. The validated models were then integrated into a comprehensive MBD model of a front-loading washing machine. This model was further verified by comparing its predicted vibrations with experimental results obtained from actual washing machines. A parametric study assessed the model's accuracy under various unbalanced mass conditions and revolutions per minute ranges, which revealed that the model is capable of generalization across different operating scenarios. Although some errors remain in specific cases involving phase differences, the overall average error is 20.11%, with a standard deviation of 4.10%. These results demonstrate that the proposed framework effectively captures the vibration behavior of front-loading washing machines, offering a reliable tool for enhancing design and operational efficiency.

1 | Introduction

Accurately predicting the vibration behavior of a front-loading washing machine is crucial for its design and development, as it enables manufacturers to create machines that can operate more quietly, smoothly, and reliably, thereby enhancing user experience and safety. A front-loading washing machine consists of several key components, schematically represented in Figure 1. To analyze these components, multibody dynamics (MBD), a branch of mechanics focused on systems composed of multiple interconnected rigid or flexible bodies, is often employed [1–4]. MBD simulations model the complex interactions between various components of the washing machine, providing valuable insights into potential sources of vibration and allowing for more precise control over the machine's operational behavior.

Recently, numerous studies have utilized MBD simulations to predict vibrations in washing machines [5–10]. Fundamental analyses have been conducted to identify the components that most significantly impact vibration behavior. In particular, extensive research has focused on modeling methods for the damper, a critical component that influences vibration, underscoring its importance in the vibration analysis of front-loading washing machines [11–14]. The damper plays a vital role in minimizing vibrations generated during the washing machine's

---

https://doi.org/10.1002/msd2.70009

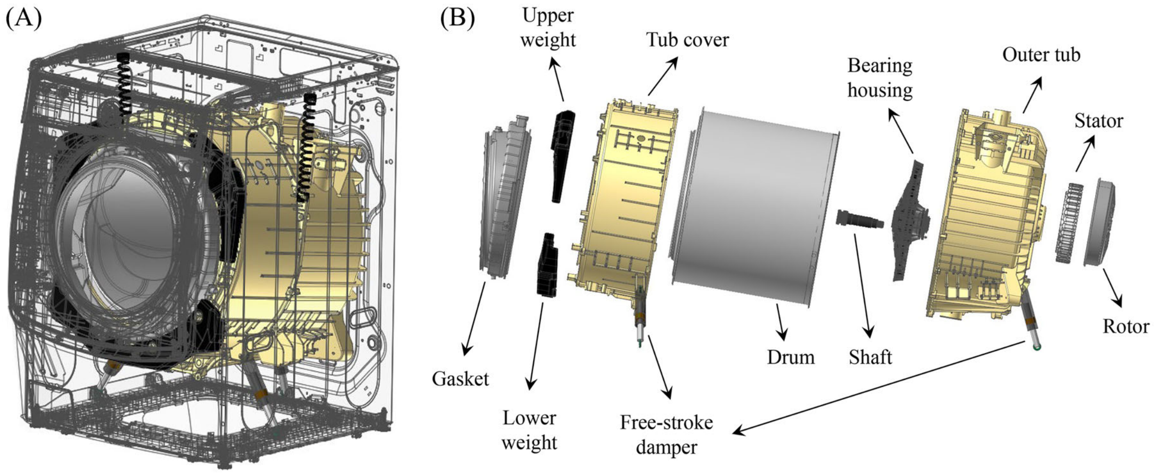

FIGURE 1 | Illustrative schematic of the front-loading washing machine: (A) the three-dimensional modeling and (B) the main components.

operation, especially during the spin cycle, where high-speed drum rotation and uneven load distribution, such as wet clothing, create substantial unbalanced forces. The damper absorbs and dissipates these forces, reducing vibrations transmitted to the machine's structure and the surrounding environment [9–12].

Conventional methods, such as the finite element method (FEM), have been used to model dampers and accurately determine vibration characteristics [13–16]. However, although FEM provides highly accurate simulations of complex systems, it is often computationally intensive and time-consuming, making it less suitable for real-time analysis or situations with limited computational resources. Consequently, recent studies have focused on developing simpler yet accurate mathematical models that balance computational efficiency with prediction accuracy [11, 12]. Despite advancements in damper modeling research, the vibration of an assembled washing machine is accurately predicted only under specific unbalanced mass conditions, and no existing model demonstrates high accuracy across a range of unbalanced mass conditions or varying revolutions per minute (RPM) levels. This indicates that precise modeling of the connecting components made of rubber materials, such as the connecting bushing that links the damper to the tub and the gasket that connects the door to the tub, is essential for developing a generalized model [7, 10].

This study presents a novel computational framework for accurately predicting the vibration of front-loading washing machines. First, to identify the dynamic characteristics of key components, such as dampers, connecting bushings, and gaskets, which significantly influence front-loading washing machines, experimental methods and conditions for each component are proposed. Second, mathematical modeling for each component is developed, and parameter identification is performed based on unit-level experimental results. The models of each unit are validated by comparing the mathematical model results with optimized parameters to experimental data. Finally, the MBD model of a front-loading washing machine was constructed by integrating the validated units and is further verified by comparing it with experimental results from actual washing machines. To account for various unbalanced mass conditions, parametric analysis is performed using the front unbalanced mass, rear unbalanced mass, and the phase difference between these two masses. Additionally, to verify vibration accuracy under various RPM conditions during the spin cycle, the RPM profile was divided into eight regions, and the model was validated by comparing the root mean square (RMS) values of the vibrations for each section [17].

The rest of paper is organized as follows. Section 2 presents the component-level experiments conducted on a front-loading washing machine, including the experimental methods, conditions, and responses of each component, such as the free-stroke damper, connecting bushing, and gasket, which are used to validate the mathematical modeling. Section 3 outlines the mathematical modeling approach for each component, along with the parameter identification procedure and the model verification results. The vibration experimental method for an actual front-loading washing machine is introduced in Section 4, where the vibration responses of the washing machine model, developed by integrating the mathematical models, are compared with identify parameters that could not be obtained from the component-level experiments and to evaluate the performance of the simulation. Finally, conclusions are drawn in Section 5.

2 | Component-Level Experiments of the Front-Loading Washing Machine

In this section, experiments are presented to extract the physical characteristics of components in a front-loading washing machine. As depicted in Figure 2, the components that most significantly affect the vibration of the washing machine are the free-stroke damper, the connecting bushing between the damper and tub, and the gasket. The damper features a free-stroke region to isolate vibrations from unbalanced drum rotation. The connecting bushing is crucial for providing flexibility, damping, and realistic joint behavior between the damper and the tub. The gasket in a washing machine creates a waterproof seal between the door and the drum to prevent water leakage during operation and cushions the connection to reduce vibrations. In the following subsections, the experiments for each component are detailed, and the characteristics required to

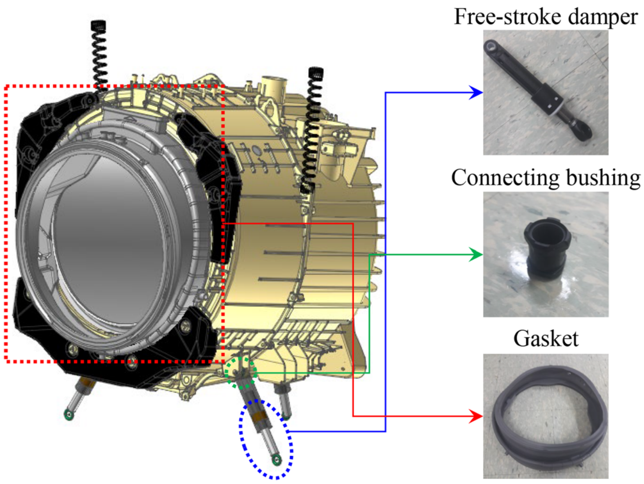

FIGURE 2 | The components that most significantly affect the vibration of the washing machine.

validate the mathematical modeling of each component are explained. The maximum RPM of the spin cycle is 350 RPM, equivalent to 5.83 Hz, and the goal is to develop a dynamic model capable of predicting vibrations during this cycle. In the component-level experiments, the maximum frequency for the damper and connecting bushing was set to 7 Hz, while the gasket was limited to 5 Hz. Various displacements were selected based on the frequency, and experiments were conducted using several displacements within the maximum amplitude that the MTS equipment could reliably handle. Notably, because the gasket is a relatively bulky component, it becomes challenging to stably measure the reaction force even with small displacements at frequencies exceeding 5 Hz. Therefore, its characteristics were extracted to the 5 Hz range. All results have been normalized to the criterion to maintain internal company confidentiality.

2.1 | Physical Test of a Free-Stroke Damper

The free-stroke damper consists of an outer tube, an inner tube, and a sponge, as illustrated in the cross-sectional view in Figure 3. The leading causes of friction in a free-stroke damper can be categorized into three types: basic friction, main friction, and deformation friction. First, the basic friction is caused by structural contact between the outer and inner tubes and the oil's viscosity. Second, the main friction results from structural contact between the sponge and the inner tube and the oil's viscosity. Finally, the deformation friction arises from the reaction force due to sponge deformation between the sponge and the outer tube. This friction is a force that occurs after the free-stroke region.

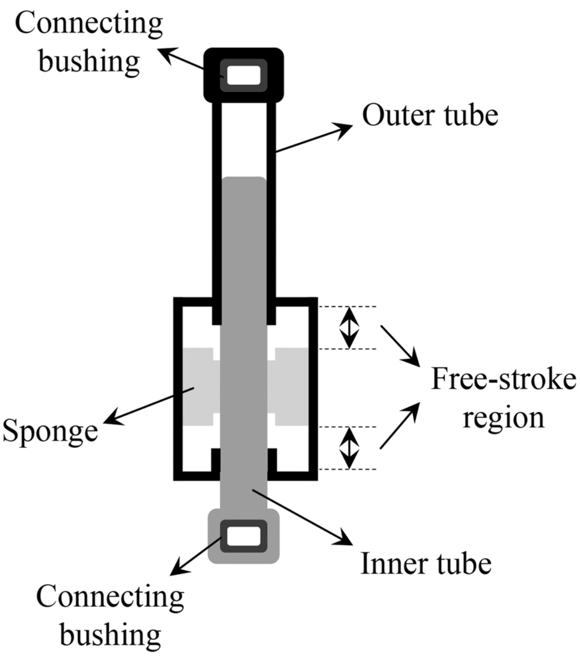

FIGURE 3 | The cross-sectional illustration of the structure of a free-stroke damper.

FIGURE 4 | The free-stroke damper test using a uniaxial test system.

To determine the characteristics of the damper, a uniaxial test system is used in the experiment, as shown in Figure 4. The outer tube of the damper is fixed. In contrast, the equipment connected to the inner tube moves axially according to the specified excitation conditions. Harmonic displacements, expressed as $d(t) = A \cdot \sin(2\pi ft)$, are applied to the damper as combinations of several frequencies ($f \in [1, 7]$ Hz) and amplitudes ($A \in [1, 10]$ mm). This experimental setup allows for systematically investigating the damper's behavior under different dynamic loading scenarios.

Figure 5 presents the time–response and force–displacement curves for the free-stroke damper test conducted at $f = 3$ Hz and $A = 10$ mm. The curve initiates at point A and forms a loop. The segment from point A to point B represents the free-stroke region, where the sponge remains undeformed. Between points B and C, the force increases as the sponge undergoes deformation. At point C, the maximum damping force is reached, and the damper transitions from tension to

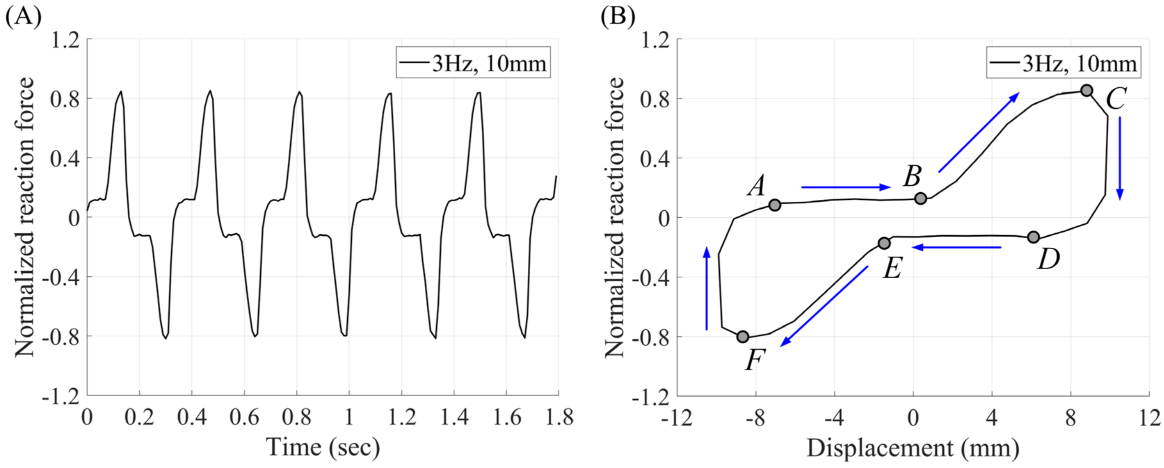

FIGURE 5 | (A) The time–response and (B) force–displacement diagram of the free-stroke damper test at excitation frequency $f = 3$ Hz and amplitude $A = 10$ mm.

compression at point *D*. Subsequently, the operation mirrors the reverse process described earlier.

2.2 | Physical Test of a Connecting Bushing

The connecting bushing links the tub and the damper, permitting free movement while simultaneously providing rigidity and damping. As depicted in Figure 6, the connecting bushing exhibits six degrees of freedom, encompassing three translational motions and three rotational motions. Due to the axial symmetry of the bushing, its characteristics along the *x*- and *y*-axes are identical.

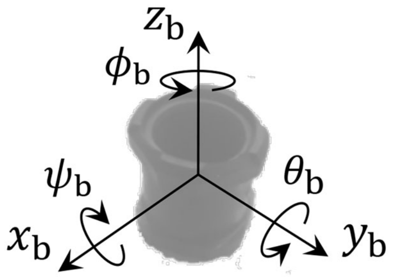

FIGURE 6 | Six degrees of freedom in connecting bushing, including three translational motions and three rotational motions.

To determine the characteristics of the connecting bushing, three types of experiments are conducted, as shown in Figure 7. In the first and second experiments, the connecting bushing is fixed to a jig to measure the translational reaction forces in the radial and axial directions. Similar to the free-stroke damper, the excitation is applied at various frequencies ($f \in [1, 7]$ Hz) and amplitudes ($A \in [0.1, 4]$ mm), and the corresponding forces F_{x_b}, F_{y_b}, and F_{z_b} are measured. The small displacement applied, as opposed to the experiment with the free-stroke damper, is due to the limited deformation of the rubber during the actual operation of the washing machine. Figure 8 shows the time–response and force–displacement curves for the connecting bushing test conducted at $f = 5$Hz. In the force–displacement curve, a monotonically increasing trend of stiffness is observed in both the radial and axial directions. In particular, it can be observed that the radial direction increases more sharply.

The third experiment is designed to apply moments to extract the connecting bushing's rotational characteristics. These characteristics are determined by calculating the moments, which involve multiplying the measured reaction forces by the corresponding arm $R = 100$ mm of the jig and the kinematically calculated rotation angle. Figure 9 shows the time–response and force–angle curves for the connecting bushing test conducted at $f = 5$Hz. From the force–angle curve, a monotonous increasing trend in stiffness can be seen, similar to the previous experiment. Axial rotation is predominantly governed by friction, making it difficult to characterize experimentally. Consequently, we utilize mathematical modeling to identify the parameters that define the system.

2.3 | Physical Test of a Gasket

The gasket serves as a connector between the tub and the front door, facilitating free movement while providing stiffness and damping. As depicted in Figure 10, the gasket exhibits six degrees of freedom, including three translational and three rotational motions, similar to the connecting bushing. The gasket is assumed to be axisymmetric, indicating that its properties are identical along both the *x*- and *y*-axes.

To confirm the characteristics of the gasket, two types of experiments are conducted, as illustrated in Figure 11. In the first experiment, the gasket is fixed on a jig, and the translational reaction forces in the *x*- and *y*-directions are measured. In the second experiment, the translational reaction force in the *z*-direction is measured. Measuring the rotational reaction force is challenging due to the rapid shape change of the gasket; therefore, its characteristics are derived from a mathematical model through parameter identification. Various frequencies

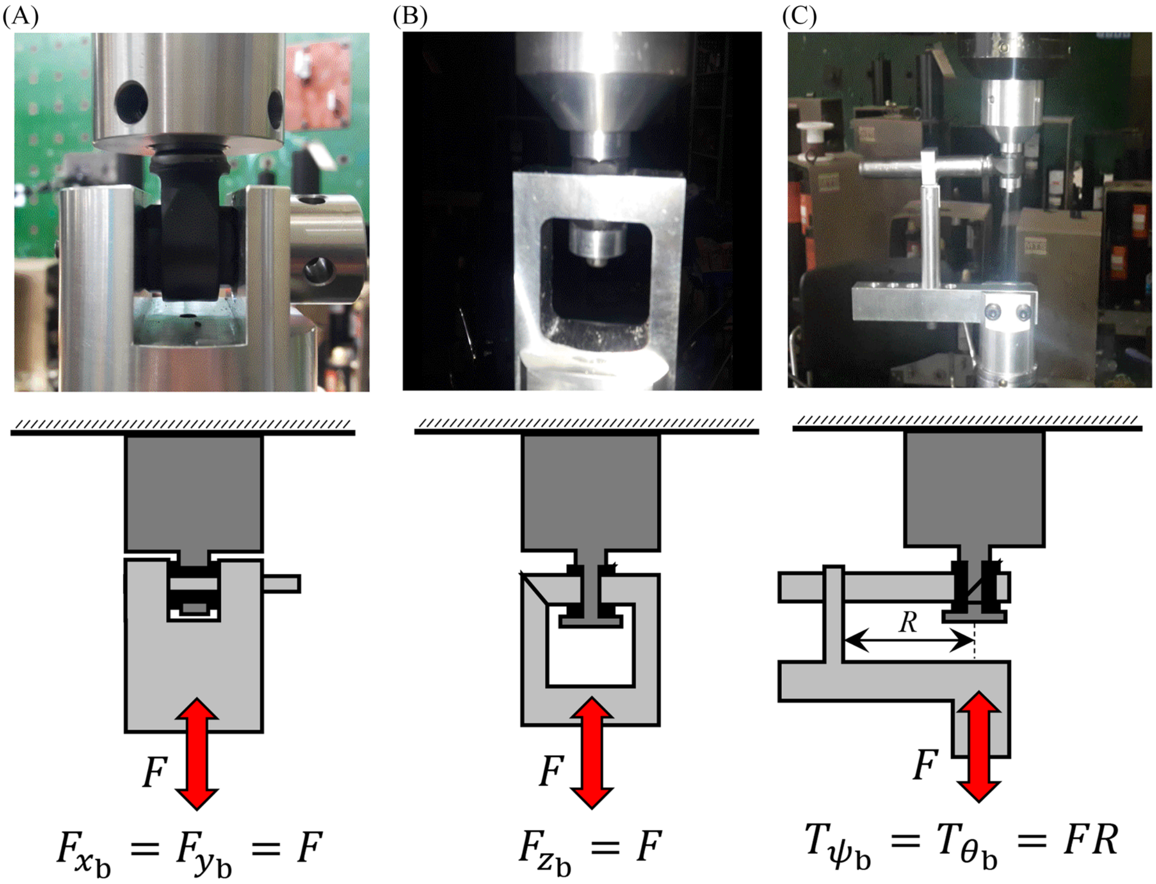

FIGURE 7 | Experimental methods for determining the characteristics of the connecting bushing: (A) radial reaction force, (B) axial reaction force, and (C) rotational reaction force.

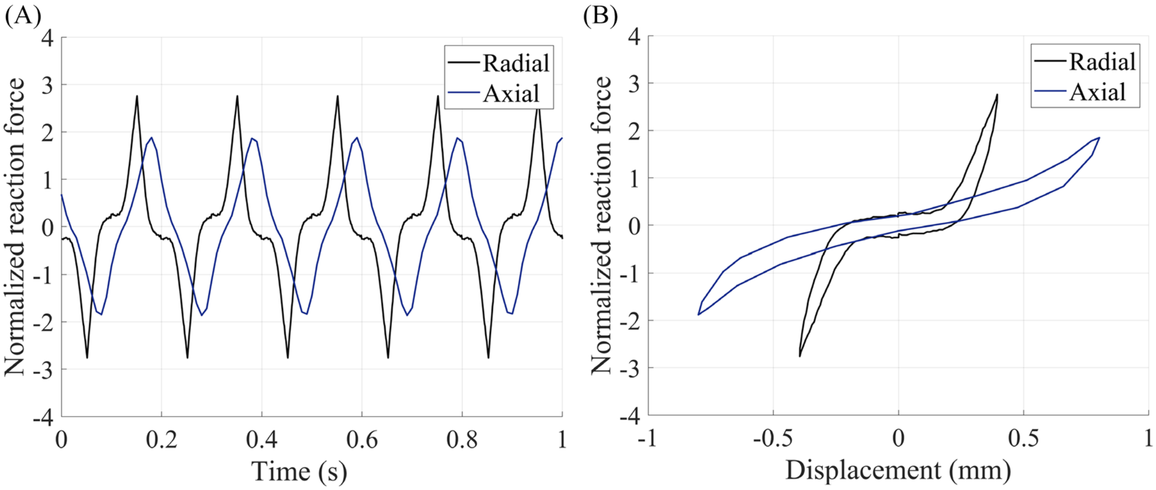

FIGURE 8 | (A) The time–response and (B) force–displacement diagram of the connecting bushing test for radial and axial reaction forces.

($f \in [1, 5]\,\mathrm{Hz}$) and amplitudes ($A \in [1, 10]\,\mathrm{mm}$) are used for excitation, and the corresponding forces F_{x_g}, F_{y_g}, and F_{z_g} are recorded. Figure 12 represents the time–response and force–displacement curves for the gasket test conducted at $f = 3\,\mathrm{Hz}$. The force–displacement curve reveals a linear trend of increasing stiffness in both radial and axial directions. Notably, the stiffness is greater in the radial direction, as indicated by the steeper slope. The gasket has a complex and thin shape, which makes it challenging to measure the load uniformly during rotation. Therefore, instead of conducting a single-item experiment, the characteristics were determined through parameter identification using mathematical modeling for the rotation direction of the gasket in the verification of an actual washing machine model.

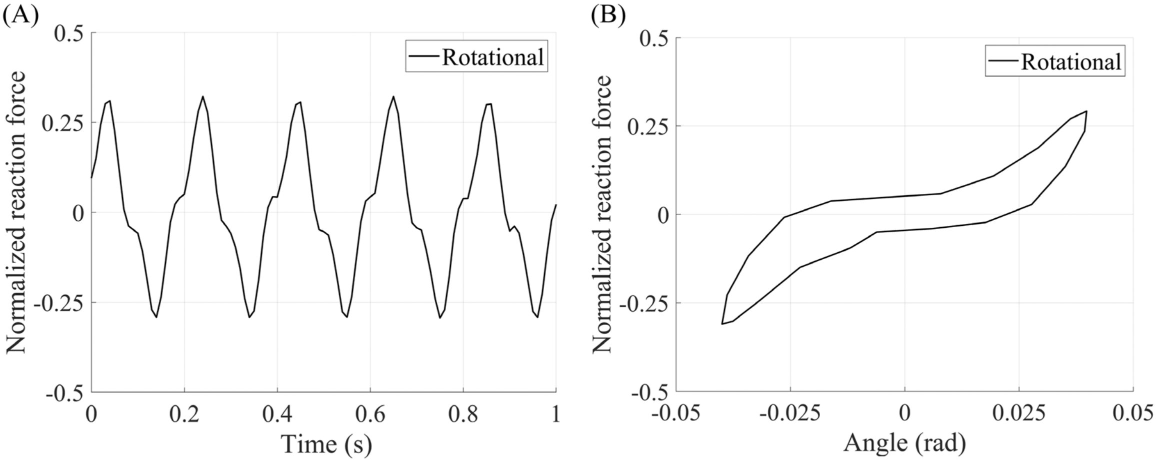

FIGURE 9 | (A) The time–response and (B) force–angle diagram of the connecting bushing test for rotational reaction force.

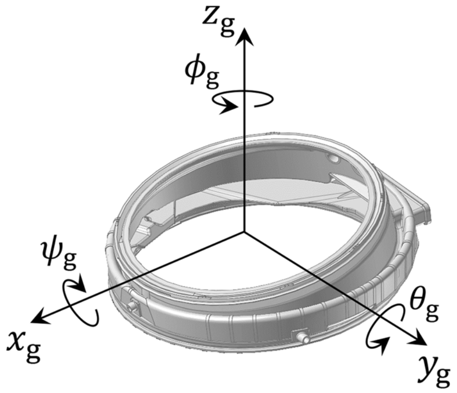

FIGURE 10 | Six degrees of freedom of the gasket, including three translational motions and three rotational motions.

3 | Component-Level Mathematical Model of the Front-Loading Washing Machine

This section introduces a simplified mathematical model to reduce computational effort while accurately representing the key characteristics of the main components, including the free-stroke damper, connecting bushing, and gasket. An essential aspect of developing an accurate mathematical model is the identification of model parameters. The model parameters are adjusted so that the model results closely match the actual experimental data. One of the optimization techniques, the response surface method [18, 19], is adopted to minimize the difference between the model results and experimental data. The objective function e is the root mean square error (RMSE) between the experiment and the model results, which can be formulated as follows:

$$e = \sqrt{\frac{1}{n}\sum_{i=1}^{n}\left[F_{\mathrm{exp}} - F_{\mathrm{sim}}\right]^2}, \tag{1}$$

where n is the number of data points; F_{exp} and F_{sim} are the experimentally measured reaction force and calculated reaction force by a mathematical model, respectively. Once the model parameters are optimized, the mathematical model is verified based on the RMSE.

3.1 | Mathematical Modeling and Validation of a Free-Stroke Damper

To build a mathematical model for the free-stroke damper, a free-body diagram is defined as shown in Figure 13.

The basic friction force f_b refers to the friction between the inner and outer tubes. This force always occurs regardless of the free-stroke region, and its equation can be expressed as [20, 21]

$$f_b = \mathrm{HAVSIN}(\dot{x}_o - \dot{x}_i, -v_b, p_b, v_b, -p_b), \tag{2}$$

where HAVSIN function is defined as follows:

$$\mathrm{HAVSIN}(x, x_0, h_0, x_1, h_1) = \begin{cases} h_0, & x \le x_0, \\ \dfrac{h_0 + h_1}{2} + \dfrac{h_0 - h_1}{2}\sin\left(\dfrac{x - x_0}{x_1 - x_0} - \dfrac{\pi}{2}\right), & x_0 \le x \le x_1, \\ h_1, & x \ge x_1, \end{cases} \tag{3}$$

The HAVSIN function processes changes over the interval (x_0–x_1) using a sine wave, ensuring smooth and continuous transitions without abrupt changes. Additionally, it is not only continuous but also differentiable within the defined interval. The parameters v_b and p_b for basic friction are determined experimentally. The main friction force f_m represents the friction between the inner tube and sponge. This force is defined using the modified stick transition velocity friction model, which considers the motion of the sponge as follows:

$$f_m = \begin{cases} -\mathrm{sgn}(\dot{x}_s)\cdot\left(f_{\max} + C_m\dot{x}_s\right), & |\dot{x}_s| \ge |\dot{x}_o - \dot{x}_s|, \\ \dfrac{f_{\max} + C_m\dot{x}_s}{|\dot{x}_o - \dot{x}_s| + \varepsilon}\dot{x}_s, & |\dot{x}_s| < |\dot{x}_o - \dot{x}_s|. \end{cases} \tag{4}$$

The parameters $f_{\max}$ and C_m for main friction are determined experimentally, and $\varepsilon = 0.001$ is used. The friction force f_d arises from the deformation of the sponge between the sponge and the outer tube in the non-free-stroke region. Since the load–deformation relationship of the sponge is nonlinear, it is determined experimentally, and the friction force is defined as

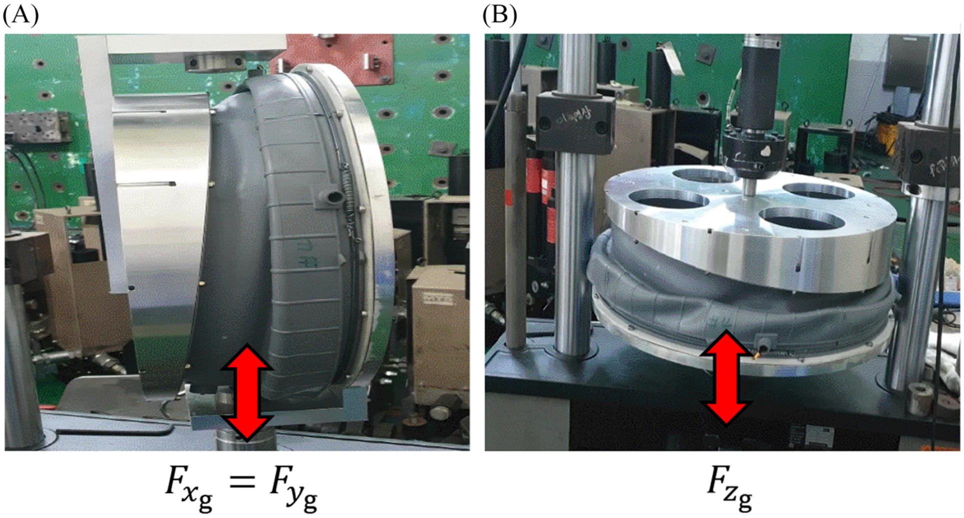

FIGURE 11 | Experimental methods for determining the characteristics of the gasket: (A) radial reaction force and (B) axial reaction force.

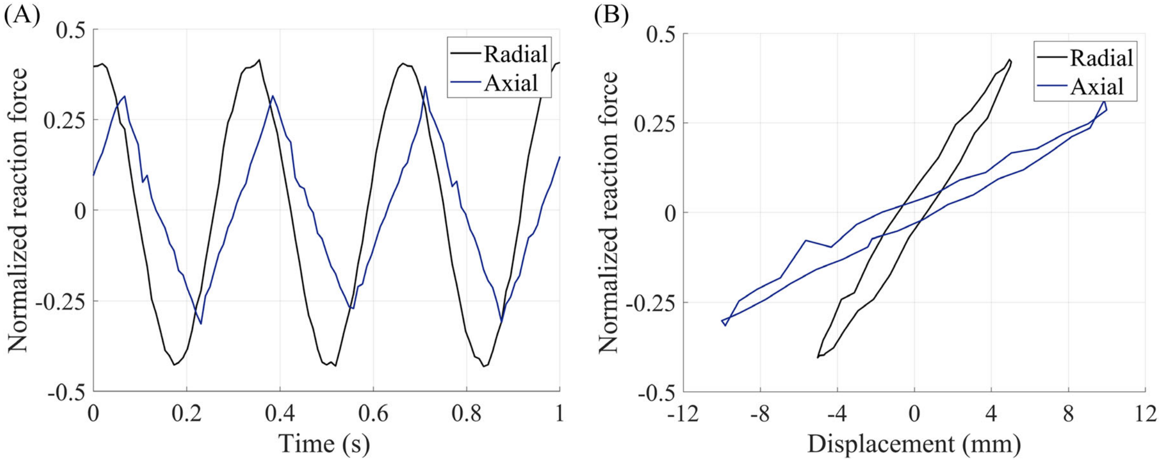

FIGURE 12 | (A) The time–response and (B) force–displacement diagram of the gasket test for radial and axial reaction forces.

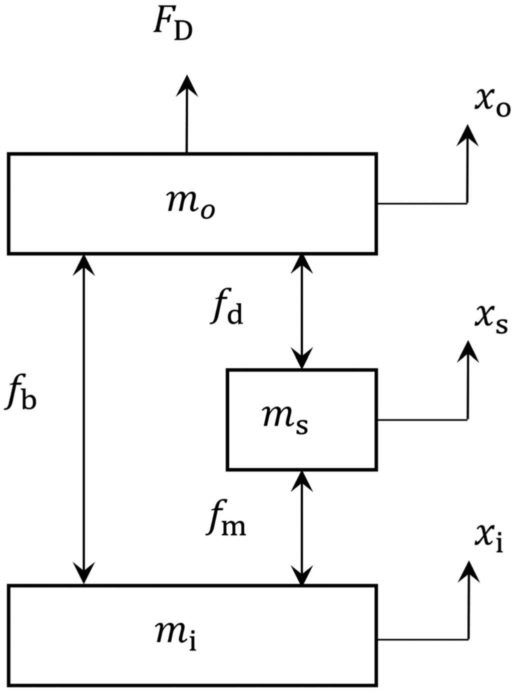

FIGURE 13 | A free-body diagram of free-stroke damper.

$$f_d = K(\delta) \cdot \delta, \tag{5}$$

where $\delta = x_o - x_s$ is the deformation of the sponge and $K(\delta)$ is the nonlinear stiffness of the sponge. On the basis of the defined friction forces, the equilibrium equation can be defined as follows:

$$\begin{cases} m_o\ddot{x}_o + m_s\ddot{x}_s + f_b - F_D = 0 \quad \text{(free-stroke region)}, \\ m_o\ddot{x}_o + f_d + f_b - F_D = 0, \quad m_s\ddot{x}_s - f_d + f_m = 0 \\ \qquad\qquad\qquad\qquad \text{(non-free-stroke region)}, \end{cases} \tag{6}$$

where m_o, m_s, m_i denote the masses of the outer tube, the sponge, and the inner tube, respectively. $x, \dot{x}, \ddot{x}$ represent displacement, velocity, and acceleration, respectively, and subscripts define each component.

To identify the parameters of the free-stroke damper, the model is optimized by minimizing RMSE using Equation (1). The optimized parameters obtained from this process are presented in Table 1. The simulation results utilizing these optimized parameters are compared with the actual experimental test results, as shown in Figure 14 and Table 2. Although RMSE for the 5 and 7 Hz is larger than those for the 1 and 3 Hz, RMSE remains within 10% of the damper's maximum reaction force. Therefore, this mathematical model is robust, showing good agreement with the experimental results conducted under various conditions.

3.2 | Mathematical Modeling and Validation of a Connecting Bushing

The connecting bushing can be modeled as a joint with six degrees of freedom, as depicted in Figure 15. The translational reaction force of the connecting bushing is determined by the product of the variation of displacement and the corresponding stiffness. The rotational reaction force is calculated by the product of the rotational angle and the respective stiffness, excluding rotational freedom about the y-axis. To represent the friction characteristics of the rotational degree of freedom at the interface between the damper and the washing machine, a friction force similar to the damper's basic friction force is added. The reaction force $\boldsymbol{F}_{\mathrm{B}}$ of connecting bushing can be expressed as follows:

$$\boldsymbol{F}_{\mathrm{B}} = \begin{bmatrix} -F_{x_{\mathrm{b}}} \\ -F_{y_{\mathrm{b}}} \\ -F_{z_{\mathrm{b}}} \\ -T_{\psi_{\mathrm{b}}} \\ -T_{\theta_{\mathrm{b}}} \\ -T_{\phi_{\mathrm{b}}} \end{bmatrix} = \begin{bmatrix} -k_{x_{\mathrm{b}}}\Delta x_{\mathrm{b}} - c_{x_{\mathrm{b}}}\Delta \dot{x}_{\mathrm{b}} \\ -k_{y_{\mathrm{b}}}\Delta y_{\mathrm{b}} - c_{y_{\mathrm{b}}}\Delta \dot{y}_{\mathrm{b}} \\ -k_{z_{\mathrm{b}}}\Delta z_{\mathrm{b}} - c_{z_{\mathrm{b}}}\Delta \dot{z}_{\mathrm{b}} \\ -k_{\psi_{\mathrm{b}}}\Delta\psi_{\mathrm{b}} - c_{\psi_{\mathrm{b}}}\Delta\dot{\psi}_{\mathrm{b}} - \mathrm{HAVSIN} \\ (\Delta\dot{\psi}_{\mathrm{b}}, -v_{\psi_{\mathrm{b}}}, -p_{\psi_{\mathrm{b}}}, v_{\psi_{\mathrm{b}}}, p_{\psi_{\mathrm{b}}}) \\ -k_{\theta_{\mathrm{b}}}\Delta\theta_{\mathrm{b}} - c_{\theta_{\mathrm{b}}}\Delta\dot{\theta}_{\mathrm{b}} - \mathrm{HAVSIN} \\ (\Delta\dot{\theta}_{\mathrm{b}}, -v_{\theta_{\mathrm{b}}}, -p_{\theta_{\mathrm{b}}}, v_{\theta_{\mathrm{b}}}, p_{\theta_{\mathrm{b}}}) \\ -\mathrm{HAVSIN}(\Delta\dot{\phi}_{\mathrm{b}}, -v_{\phi_{\mathrm{b}}}, -p_{\phi_{\mathrm{b}}}, v_{\phi_{\mathrm{b}}}, p_{\phi_{\mathrm{b}}}) \end{bmatrix}, \tag{7}$$

TABLE 1 | Optimized parameters of the free-stroke damper.

Parameters	Optimized value
v_{b} (mm/s)	90.0
p_{b} (N)	10.5
$f_{\max}$ (N)	35.0
C_{m} (Ns/mm)	0.06

TABLE 2 | RMSE of reaction forces of the free-stroke damper for each frequency and amplitude.

Frequency (Hz)	Amplitude (mm)	RMSE
1	6	0.0298
	8	0.0303
	10	0.0317
3	6	0.0272
	8	0.0278
	10	0.0296
5	1	0.0453
	3	0.0491
	5	0.0616
7	1	0.0517
	3	0.0523
	5	0.0622

Abbreviation: RMSE, root mean square error.

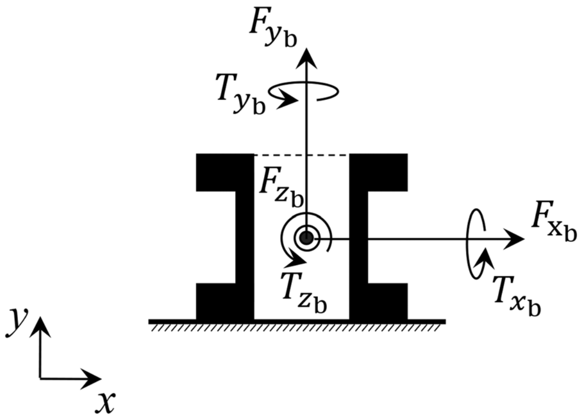

FIGURE 15 | Schematic diagram of the connecting bushing for six degrees of freedom.

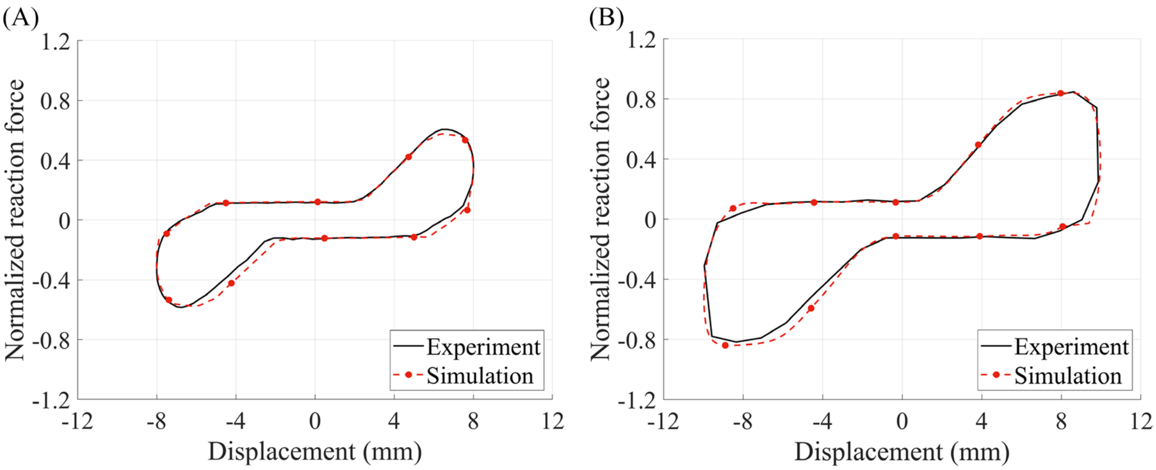

FIGURE 14 | Comparison of reaction forces versus displacement from experiments and mathematical models at (A) frequency $f = 1$ Hz and $A = 8$ mm and (B) frequency $f = 3$Hz and $A = 10$ mm.

where $k_{(\cdot)}$ is the stiffness for each axis, which is experimentally determined and can describe both linear and nonlinear characteristics. $\Delta(\cdot)$ is the change in displacement or angle of coordinates $[x_\mathrm{b}, y_\mathrm{b}, z_\mathrm{b}, \psi_\mathrm{b}, \theta_\mathrm{b}, \phi_\mathrm{b}]$ for six degrees of freedom. Also, the threshold velocity vector $\boldsymbol{v}_\mathrm{b} = [v_{\psi_\mathrm{b}} \quad v_{\theta_\mathrm{b}} \quad v_{\phi_\mathrm{b}}]^\mathrm{T}$ and the damping force vector $\boldsymbol{p}_\mathrm{b} = [p_{\psi_\mathrm{b}} \quad p_{\theta_\mathrm{b}} \quad p_{\phi_\mathrm{b}}]^\mathrm{T}$ are determined experimentally.

Similar to the approach used for the free-stroke damper, the model is optimized by minimizing the RMSE using Equation (1) to determine the parameters of the connecting bushing. The optimized parameters for the connecting bushing are listed in Table 3. It should be noted that the stiffness in the y-direction exhibits significant nonlinearity; therefore, the median curve f_{y_b} from the experimental hysteresis data is utilized in the mathematical model. The radial and axial reaction forces computed by the mathematical model, using these optimized parameters, are compared with the experimental test results, as shown in Figure 16 and Table 4. The RMSE is within 0.3, representing 10% of the maximum reaction force for the connecting bushing. The rotational reaction force is compared with the experiment results as shown in Figure 17 and Table 5. Similarly, it is confirmed that the RMSE is within 10% of the maximum reaction force.

TABLE 3 | Optimized parameters of the connecting bushing.

Parameters	Optimized value
$k_{x_\mathrm{b}}, k_{z_\mathrm{b}}$ (N/mm)	200
$c_{x_\mathrm{b}}, c_{z_\mathrm{b}}$ (Ns/mm)	0.04
k_{y_b}	f_{y_b}
c_{y_b} (Ns/mm)	0.04
$k_{\psi_\mathrm{b}}, k_{\theta_\mathrm{b}}$ (N/rad)	750
$c_{\psi_\mathrm{b}}, c_{\theta_\mathrm{b}}$ (Ns/rad)	0.05
$v_{\psi_\mathrm{b}}, v_{\theta_\mathrm{b}}$ (mm/s)	2
$p_{\psi_\mathrm{b}}, p_{\theta_\mathrm{b}}$ (N)	80

TABLE 4 | RMSE of radial and axial reaction forces of the connecting bushing for each frequency and amplitude.

Frequency (Hz)	Amplitude (mm)	RMSE (radial)	RMSE (axial)
1	0.1	0.1172	0.2124
	0.2	0.1153	0.2167
	0.4	0.1127	0.2222
3	0.1	0.1234	0.2097
	0.2	0.1198	0.2082
	0.4	0.1221	0.2144
5	0.1	0.1302	0.1913
	0.2	0.1292	0.1988
	0.4	0.1280	0.2034
7	0.1	0.1162	0.2121
	0.2	0.1212	0.2056
	0.4	0.1267	0.2084

Abbreviation: RMSE, root mean square error.

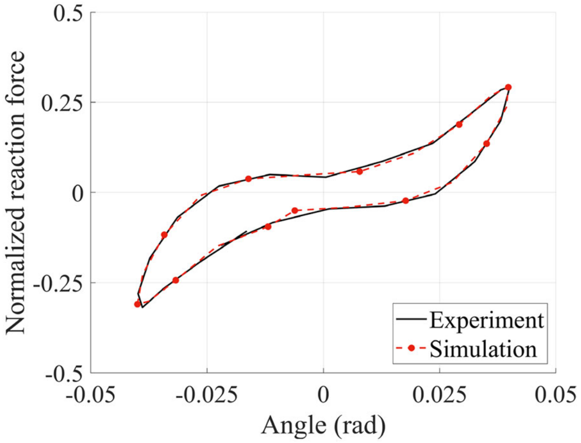

FIGURE 17 | Comparison of rotational ($f = 5\,\mathrm{Hz}$, $A = 4\,\mathrm{mm}$) reaction forces versus displacement from experiments and the mathematical model of the connecting bushing.

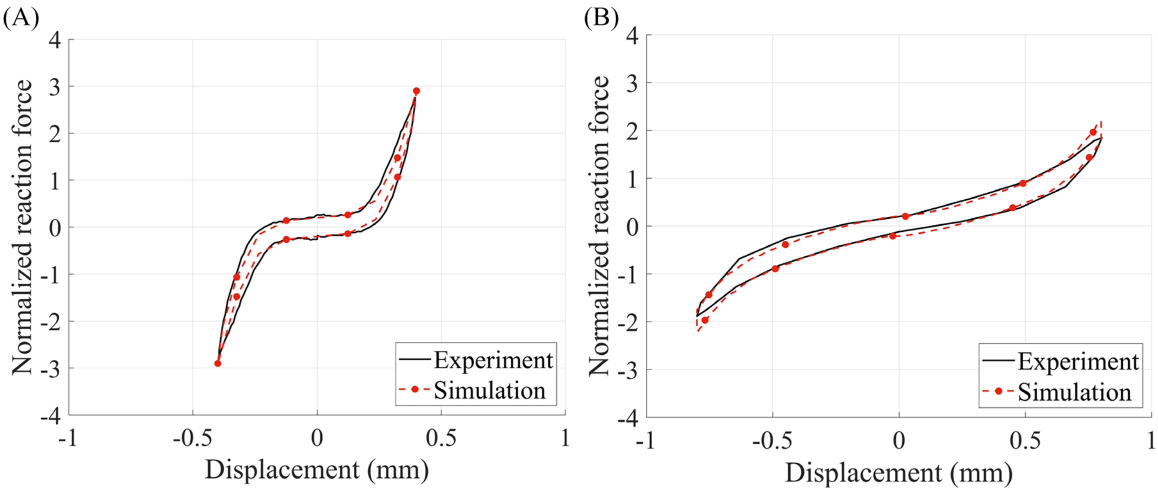

FIGURE 16 | Comparison of (A) radial ($f = 5\,\mathrm{Hz}$, $A = 0.4$ mm) and (B) axial ($f = 5\,\mathrm{Hz}$, $A = 0.8$ mm) reaction forces versus displacement from experiments and the mathematical model of the connecting bushing.

Therefore, this close agreement between the model and the experimental results under various conditions confirms the robustness of the mathematical model. In the rotational axis experiments, the buckling shape of the rubber changes during each rotational axis experiment, and thus the self-contact range also varies. In addition, buckling can induce coupled forces from deformations in multiple directions. As a result, it is experimentally difficult to extract the stiffness of the rotational axis by applying pure torsion, and it is equally difficult to achieve consistent stiffness measurements. It should be noted that the axial rotation, which is challenging to characterize experimentally, is parameterized based on the results of a comprehensive set of experiments conducted on a front-loading washing machine.

3.3 | Mathematical Modeling and Validation of a Gasket

The gasket can also be modeled as a joint with six degrees of freedom, in the same manner as the connecting bushing, as shown in Figure 18.

The translational reaction force of the gasket between the door and the tub cover is determined by the product of the variation of displacement and its stiffness, as well as the product of the rotational angle and the corresponding stiffness, except for rotational freedom about the y-axis. The damping force is applied in the same manner as the damper's basic friction force to model the frictional characteristics of the rotational degree of freedom at the interface between the door and the tub cover. The reaction force $\boldsymbol{F}_{\mathrm{G}}$ of gasket can be formulated as follows:

$$\boldsymbol{F}_{\mathrm{G}} = \begin{bmatrix} -F_{x_{\mathrm{g}}} \\ -F_{y_{\mathrm{g}}} \\ -F_{z_{\mathrm{g}}} \\ -T_{\psi_{\mathrm{g}}} \\ -T_{\theta_{\mathrm{g}}} \\ -T_{\phi_{\mathrm{g}}} \end{bmatrix} = \begin{bmatrix} -k_{x_{\mathrm{g}}}\Delta x_{\mathrm{g}} - c_{x_{\mathrm{g}}}\Delta \dot{x}_{\mathrm{g}} \\ -k_{y_{\mathrm{g}}}\Delta y_{\mathrm{g}} - c_{y_{\mathrm{g}}}\Delta \dot{y}_{\mathrm{g}} \\ -k_{z_{\mathrm{g}}}\Delta z_{\mathrm{g}} - c_{z_{\mathrm{g}}}\Delta \dot{z}_{\mathrm{g}} \\ -k_{\psi_{\mathrm{g}}}\Delta \psi_{\mathrm{g}} - c_{\psi_{\mathrm{g}}}\Delta \dot{\psi}_{\mathrm{g}} - \mathrm{HAVSIN} \\ (\Delta\dot{\psi}_{\mathrm{g}}, -v_{\psi_{\mathrm{g}}}, -p_{\psi_{\mathrm{g}}}, v_{\psi_{\mathrm{g}}}, p_{\psi_{\mathrm{g}}}) \\ -k_{\theta_{\mathrm{g}}}\Delta \theta_{\mathrm{g}} - c_{\theta_{\mathrm{g}}}\Delta \dot{\theta}_{\mathrm{g}} - \mathrm{HAVSIN} \\ (\Delta\dot{\theta}_{\mathrm{g}}, -v_{\theta_{\mathrm{g}}}, -p_{\theta_{\mathrm{g}}}, v_{\theta_{\mathrm{g}}}, p_{\theta_{\mathrm{g}}}) \\ -\mathrm{HAVSIN}(\Delta\dot{\phi}_{\mathrm{g}}, -v_{\phi_{\mathrm{g}}}, -p_{\phi_{\mathrm{g}}}, v_{\phi_{\mathrm{g}}}, p_{\phi_{\mathrm{g}}}) \end{bmatrix}. \tag{8}$$

In Equation (8), $k_{(\cdot)}$ denotes the stiffness corresponding to each axis, determined through experimental method and capable of representing both linear and nonlinear behavior. The term $\Delta(\cdot)$ indicates the variation in translational displacements and rotational angles $[x_{\mathrm{g}}, y_{\mathrm{g}}, z_{\mathrm{g}}, \psi_{\mathrm{g}}, \theta_{\mathrm{g}}, \phi_{\mathrm{g}}]$ across six degrees of freedom. Furthermore, the threshold velocity vector $\boldsymbol{v}_{\mathrm{g}} = [v_{\psi_{\mathrm{g}}} \quad v_{\theta_{\mathrm{g}}} \quad v_{\phi_{\mathrm{g}}}]^{\mathrm{T}}$ and the damping force vector $\boldsymbol{p}_{\mathrm{g}} = [p_{\psi_{\mathrm{g}}} \quad p_{\theta_{\mathrm{g}}} \quad p_{\phi_{\mathrm{g}}}]^{\mathrm{T}}$ are also derived experimentally.

The parameters of the gasket are optimized to minimize the RMSE, as described in Equation (1). The optimized parameters of the gasket are shown in Table 6. The stiffness and damping in the y-direction are approximately one-third and one-fifth of those in the x- and z-directions, respectively. Using these optimized parameters, the radial and axial reaction forces calculated from the mathematical model are compared with the experimental test results, as shown in Figure 19 and Table 7. The RMSE in the radial reaction force is within 0.2, which is within 10% of the maximum radial reaction force for the gasket. In contrast, the RMSE for the axial reaction force exceeds 0.08, which is more than 10% of the maximum reaction force. Although the complex shape of the gasket seems to have not been sufficiently experimentally tested, the vibration of the front-loading washing machine is expected to be largely unaffected by the not-matched hysteresis curve because the slope is similar. Additionally, since the rotational characteristics of the gasket are extremely challenging to extract experimentally due to its buckling shape, similar to the connecting bushing mentioned earlier, the parameters for rotation were determined through the analysis of a front-loading washing machine.

TABLE 5 | RMSE of rotational reaction forces of the connecting bushing for each frequency and amplitude.

Frequency (Hz)	Amplitude (mm)	RMSE (radial)
1	2	0.0124
	4	0.0212
3	2	0.0147
	4	0.0232
5	2	0.0144
	4	0.0233
7	2	0.0167
	4	0.0252

Abbreviation: RMSE, root mean square error.

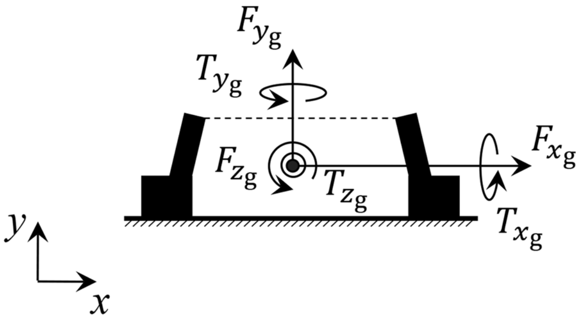

FIGURE 18 | Schematic diagram of the gasket with six degrees of freedom.

TABLE 6 | Optimized parameters of the gasket.

Parameters	Optimized value
k_{x_g}, k_{z_g} (N/mm)	8
c_{x_g}, c_{z_g} (Ns/mm)	0.05
k_{y_g} (N/mm)	3
c_{y_g} (Ns/mm)	0.01

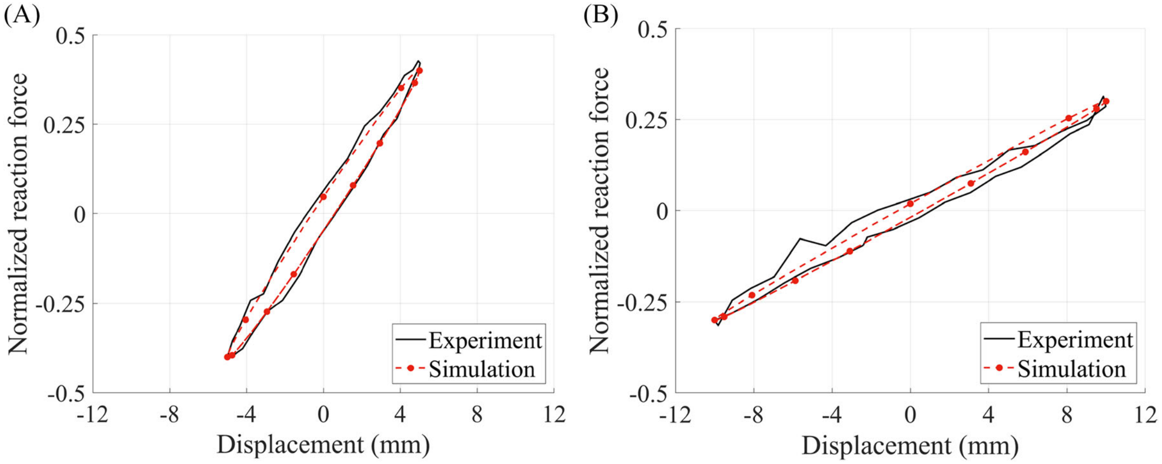

FIGURE 19 | Comparison of (A) radial ($f = 5\,\text{Hz}$, $A = 0.8$ mm) and (B) axial ($f = 5\,\text{Hz}$, $A = 0.4$ mm) reaction forces versus displacement from experiments and the mathematical model of the gasket.

TABLE 7 | RMSE of radial and axial reaction forces of the gasket for each frequency and amplitude.

Frequency (Hz)	Amplitude (mm)	RMSE (radial)	RMSE (axial)
1	1	0.0172	0.0752
	5	0.0152	0.0843
	10	0.0144	0.0892
3	1	0.0162	0.1055
	5	0.0155	0.1143
	10	0.0168	0.1037
5	1	0.0182	0.0921
	5	0.0177	0.0999
	10	0.0135	0.0946

Abbreviation: RMSE, root mean square error.

4 | Experimental Validation and Discussion

4.1 | Experiment Setup of the Front-Loading Washing Machine

An MBD model of a front-loading washing machine can be developed by integrating the mathematical models of the free-stroke damper, connecting bushing, and gasket. A graphical topology representation of the MBD model for a front-loading washing machine is presented in Figure 20. The lines representing the connections are color coded as black, blue, and green, corresponding to fixed joints, revolute joints, and springs, respectively. The tub is connected to three upper bushings through three fixed joints. Each bushing is attached to a damper via a fixed joint. The three lower bushings are anchored to the ground. The gasket is secured to the tub with a fixed joint. To enhance the stability of the tub, three weights are attached to it using fixed joints. The drum is connected to the tub through a revolute joint, allowing it to rotate relative to the tub. The motor is mounted on the drum, and the unbalanced mass is attached to the drum using a fixed joint. RecurDyn, a commercial MBD software, is used to construct the model in this study [22, 23].

To validate the model, three 3-axis accelerometer sensors are attached to the washing machine to measure acceleration, as illustrated in Figure 21 [17]. To eliminate cabinet flexibility, we simply disconnected the driving part from the entire washing machine and connected the springs and dampers to a ground jig [24]. Since the vibration of the washing machine significantly affects consumer satisfaction, particularly in relation to whether contact with the cabinet occurs, vibration is generally evaluated by displacement rather than acceleration. Consequently, the measured acceleration data are integrated twice to convert them into displacement, which is then used for model verification. To ensure internal company confidentiality, all results have been normalized to a standard criterion.

During the spin-drying cycle, significant vibrations can occur due to changes in RPM and significant unbalanced mass. To ensure that the model can accurately predict these vibrations under various conditions, it is crucial to validate it across a wide range of RPMs and unbalanced mass distributions. Consequently, this study examines the vibration of the washing machine in eight specific sections of the spin-drying profile, as depicted in Figure 21 [17]. Additionally, the configuration of the unbalanced mass was evaluated using 33 combinations in total, comprising six single-mass configurations and 27 dual-mass configurations. These combinations include a front unbalanced mass, $m_\text{f} = [200, 400, 600]$ g, a rear unbalanced mass $m_\text{r} = [200, 400, 600]$ g and a phase shift $\theta = [0, 90, 180]°$ between the two masses, as illustrated in Figure 22 [17].

4.2 | Validation of Simulation Performance With Experiment

Although many parameters are identified from the component-level experiments, the parameters of the mathematical model related to the axial rotation characteristics of the connecting bushing and the gasket's characteristics in all rotational directions could not be determined due to the complexity of the geometry and the difficulty of the experiments. Therefore, the remaining parameters are identified through a comparison of experimental and simulation results for 33 unbalanced mass configurations. The objective function for this parameter

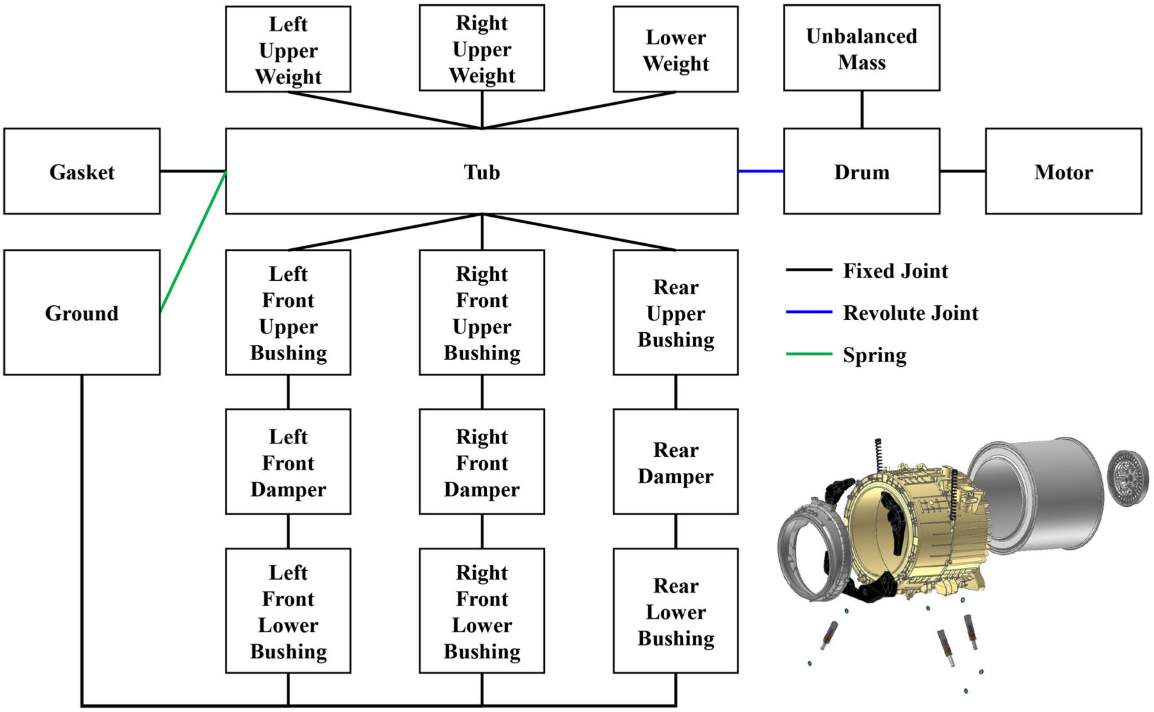

FIGURE 20 | Topological description of the multibody model of front-loading machine.

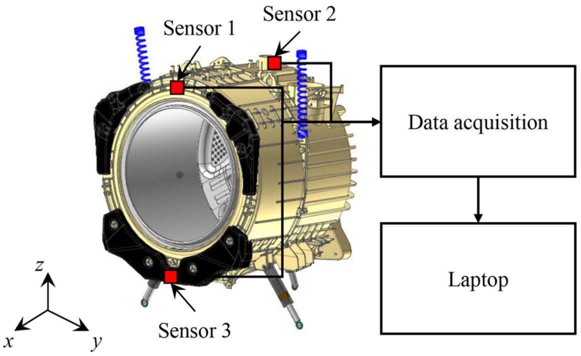

FIGURE 21 | Comprehensive multibody dynamics model and vibration measurements of a front-loading washing machine.

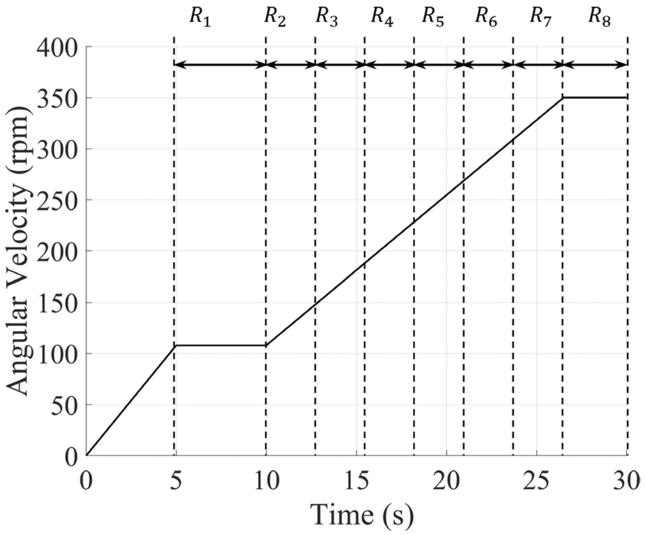

FIGURE 22 | RPM profile of the spin cycle of a front-loading washing machine. RPM, revolutions per minute.

TABLE 8 | Optimized parameters including axial rotation characteristics of the connecting bushing and gasket characteristics in all directions of rotation.

Parameters	Optimized value
v_{ϕ_b} (mm/s)	0.1
p_{ϕ_b} (N)	70
k_{ψ_g}, k_{θ_g} (N/rad)	73 000
c_{ψ_g}, c_{θ_g} (Ns/rad)	0
v_{ψ_b}, v_{θ_b} (rad/s)	1.5
p_{ψ_b}, p_{θ_b} (N)	3700
k_{ϕ_g} (N/rad)	890 000
c_{ϕ_g} (Ns/rad)	0
v_{ϕ_g} (rad/s)	1.5
p_{ϕ_g} (N)	3700

identification is defined as the relative error between the experiment and the model for the displacement in the spin-drying cycle, as follows:

$$\epsilon_{\mathrm{rel}}(R_i) = \frac{\|d_{\mathrm{rms,exp}}(R_i) - d_{\mathrm{rms,sim}}(R_i)\|}{\|d_{\mathrm{rms,exp}}(R_i)\|}, \tag{9}$$

where $d_{\mathrm{rms,exp}}$ and $d_{\mathrm{rms,sim}}$ are the displacements, which are expressed as the RMS value, for experimental and simulation results, respectively; R_i is the RPM region. Table 8 shows the parameters optimized through this process. Using these parameters, the overall accuracy is assessed by comparing the RMS of each RPM region, a representative metric, against the results from 33 simulations and corresponding experimental data.

Figure 23 represents the displacements for each RPM region when the condition of single front unbalanced mass is 400 g. The displacement trends for each sensor and direction within the RPM range match closely between the experimental and simulation results. The simulation, in particular, accurately predicts the maximum displacement in the *y*- and *z*-directions, which are crucial for evaluating potential cabinet contact.

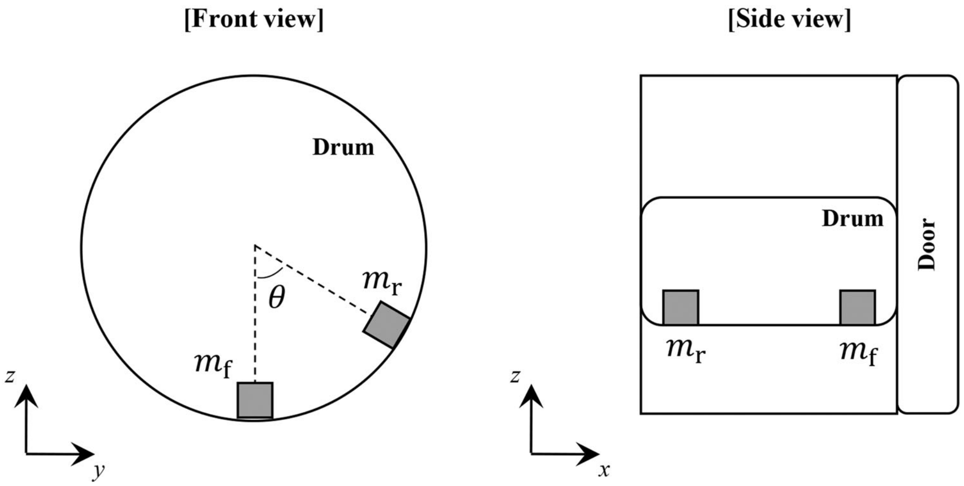

FIGURE 23 | Definition of front unbalanced mass and rear unbalanced mass and schematic representation of the phase difference between these two masses.

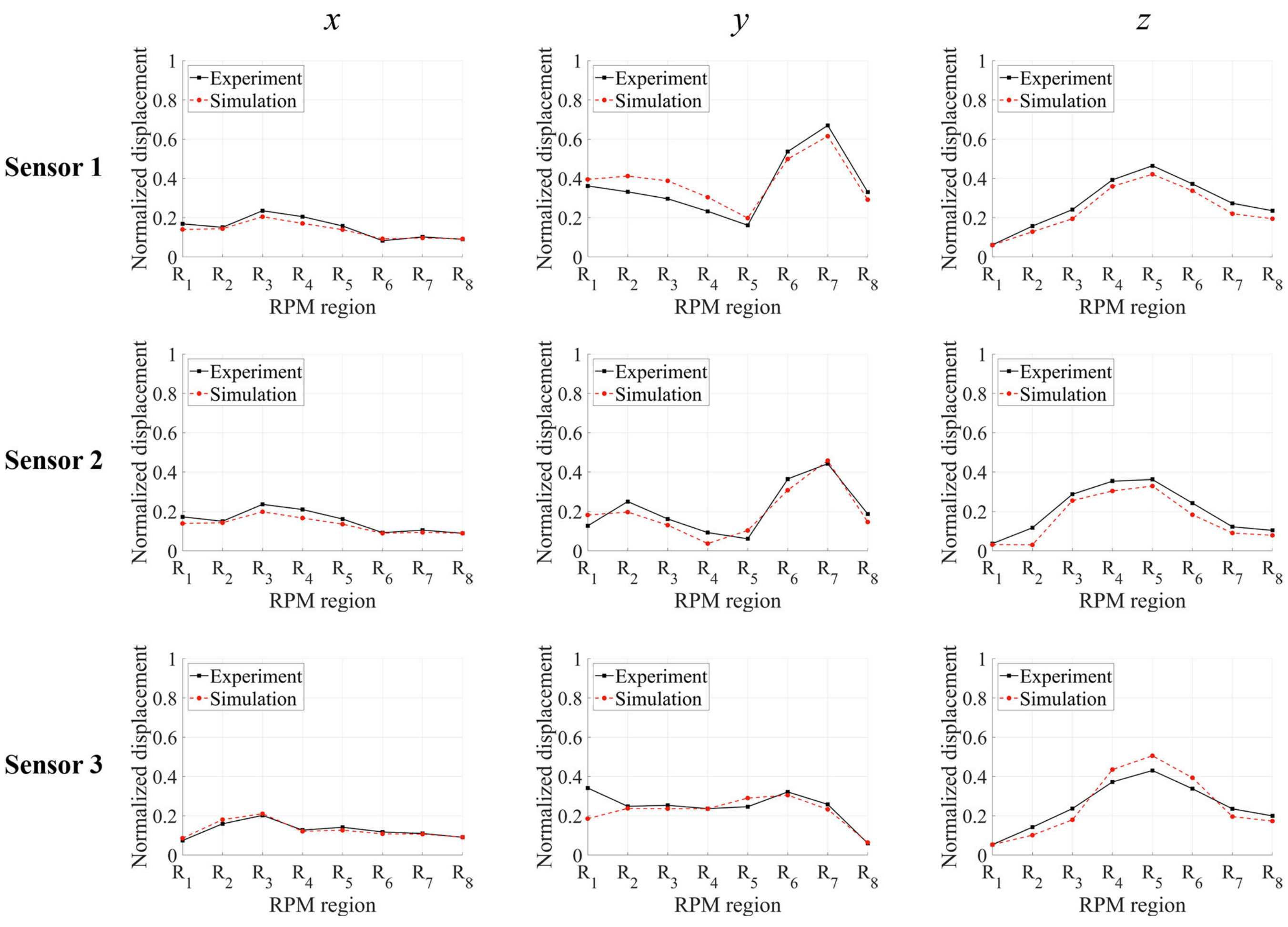

FIGURE 24 | Comparison of displacements for each RPM region and direction of sensor under the front unbalanced mass m_f is 400 g only. RPM, revolutions per minute.

The largest vibration occurs in the region R_7 in the y-direction and in the region R_5 in the z-direction, demonstrating that these are well estimated. In contrast, the displacements for each RPM region when the single rear unbalanced mass is set to 400 g are shown in Figure 24. Similarly, the experimental and simulation results closely match. It is noteworthy that the vibration is largest in the R_2 section for the y-direction displacement of the second sensor, and this characteristic trend is accurately estimated by the simulation.

To examine the effect of displacement on phase, the results are compared for the condition where the front and rear unbalanced masses are both 400 g and positioned opposite each other, corresponding to a phase of 180°, as shown in Figure 25. The displacement trends between the experimental and simulation results closely match. Notably, the vibration in the z-direction, which represents the up-and-down displacement, is significantly reduced in all sensors, demonstrating that the model accurately captures this characteristic. However, there are sections where the displacements in the x- and y-directions do not align closely, leading to a relatively larger error compared with the case with a single unbalanced mass.

For quantitative evaluation of simulation performance, the average of errors of all sensors and directions calculated using Equation (9) for all conditions is shown in Table 9. The errors for the single unbalanced mass conditions (Cases 1–6) and the two unbalanced mass conditions with a 0° phase difference (Cases 7–15) are relatively small compared with the errors for the two unbalanced mass conditions with 90° and 180° phase (Cases 16–33). The causes of this phenomenon can be broadly categorized into three factors.

First, the simulation does not account for whirling motion, an instability that causes the shaft or rotor to deviate from the centerline during rotation, resulting in lateral vibration. Ideally, the shaft should rotate precisely along its axis, but interactions between the bearing and the shaft can induce lateral vibrations, leading to circular or elliptical trajectories. This phenomenon is particularly pronounced when the two unbalanced masses are out of phase. However, in the simulation model, the drum and tub are kinematically constrained to a revolute joint, enforcing a perfectly circular trajectory and excluding whirling motion. Although incorporating contact between the bearing and the shaft could improve accuracy, it would also significantly increase computational cost.

Second, although the actual drum may not have an inherent imbalance in mass, achieving perfect balance during the machining process is not feasible, resulting in a distribution of imbalance mass. Conversely, in the simulation model, the drum is modeled to have a perfectly balanced mass (zero imbalance).

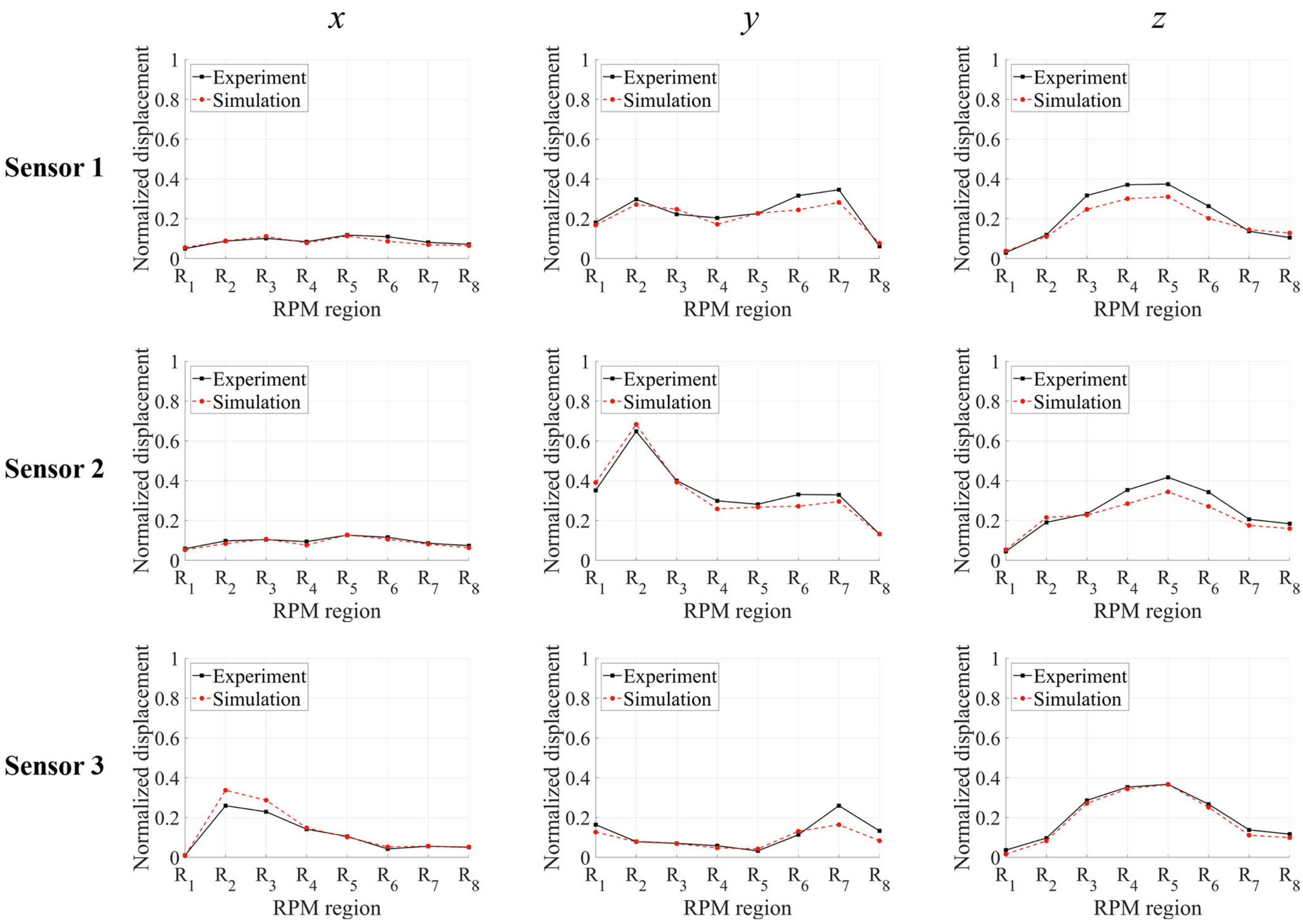

FIGURE 25 | Comparison of displacements for each RPM region and direction of sensor under the rear unbalanced mass m_r is 400 g only. RPM, revolutions per minute.

TABLE 9 | Results of the average of errors of all sensors and directions for 33 conditions related to the configuration of the unbalanced mass.

Case	Front unbalanced mass (g)	Rear unbalanced mass (g)	Phase (°)	Average error (%)
1	200	0	0	21.1
2	400	0	0	16.1
3	600	0	0	17.4
4	0	200	0	17.8
5	0	400	0	13.7
6	0	600	0	16.7
7	200	200	0	18.7
8	400	200	0	14.6
9	600	200	0	16.3
10	200	400	0	16.3
11	400	400	0	13.2
12	600	400	0	15.2
13	200	600	0	17.4
14	400	600	0	13.9
15	600	600	0	17.4
16	200	200	90	27.5
17	400	200	90	25.5
18	600	200	90	24.3
19	200	400	90	21.8
20	400	400	90	27.2
21	600	400	90	27.3
22	200	600	90	23.2
23	400	600	90	22.2
24	600	600	90	24.4
25	200	200	180	20.6
26	400	200	180	18.9
27	600	200	180	21.1
28	200	400	180	23.2
29	400	400	180	24.7
30	600	400	180	23.1
31	200	600	180	20.7
32	400	600	180	19.7
33	600	600	180	22.4

This uncertainty parameter in the actual experiment can cause errors with the simulation.

Lastly, another factor contributing to the discrepancy is the challenge of accurately measuring and aligning phase differences of 90° and 180° between the front and rear unbalanced masses in the experiments, whereas achieving a 0° phase difference is relatively straightforward. In contrast, simulations can precisely calculate and model these phase differences, which may lead to discrepancies when compared with experimental conditions.

Despite these challenges, the overall mean error and standard deviation across all conditions are approximately 20.11% and 4.10%, respectively. These results indicate that the simulation captures the characteristic trends effectively, with no significant issues in predicting the overall trends or the maximum displacement under the various conditions (Figure 26).

5 | Conclusion

In this study, a computational framework is proposed for developing an MBD model based on component-level experiments and mathematical modeling to accurately predict the vibration behavior of front-loading washing machines. The study introduces an experimental method to identify the dynamic

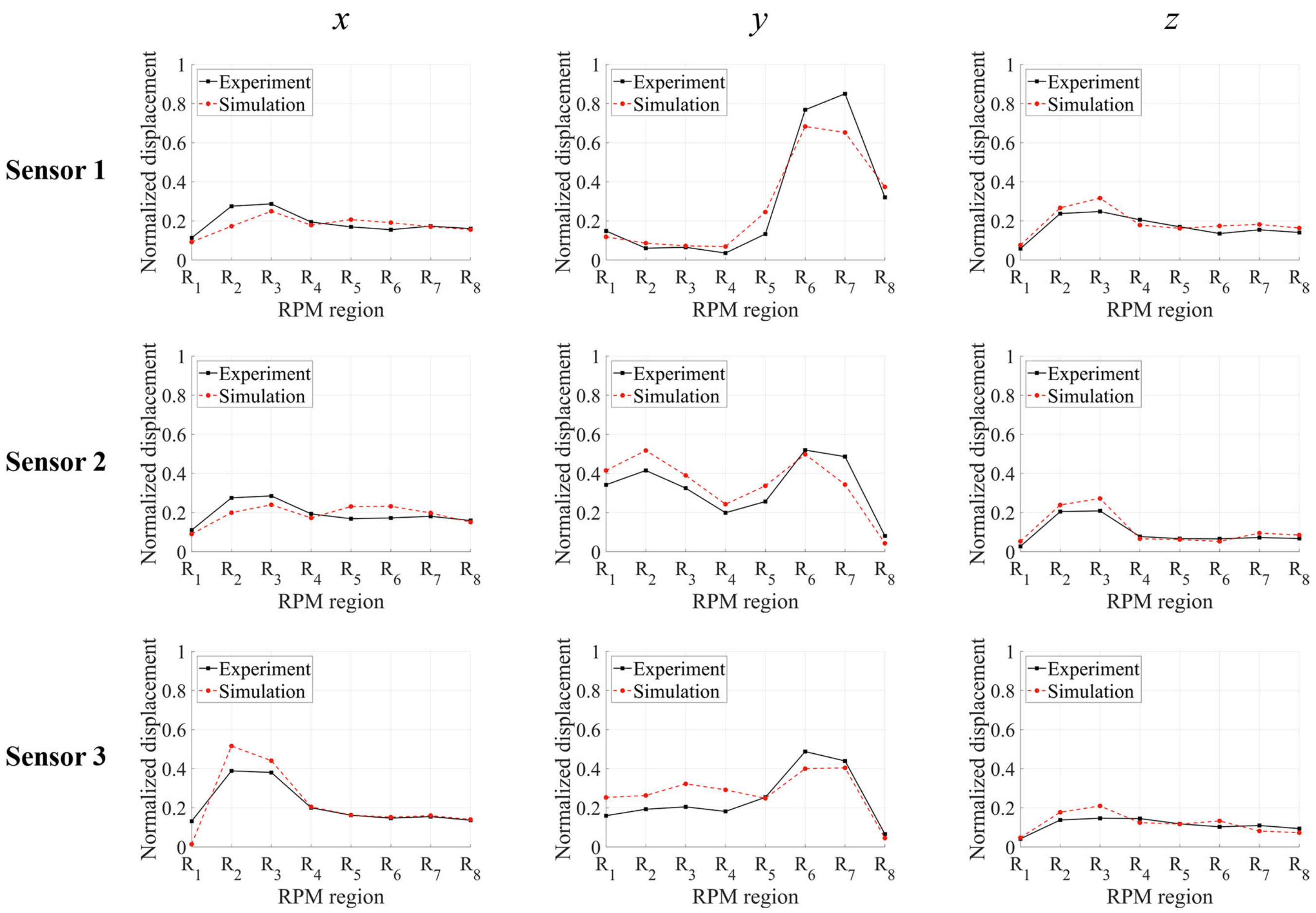

FIGURE 26 | Comparison of displacements for each RPM region and direction of sensor under the front, rear unbalanced mass $m_f = 400$ g, $m_r = 400$ g, and the phase $\theta = 180°$. RPM, revolutions per minute.

characteristics of the free-stroke damper, connecting bushing, and gasket, which are the components that most significantly affect the washing machine's vibration. Additionally, a simple yet accurate mathematical model is developed to represent these dynamic characteristics, and its accuracy is verified by comparing the model's results with experimental data from individual components. The MBD model is then constructed by integrating these validated mathematical models and further verified by comparing its predictions with the vibrations observed in an actual front-loading washing machine.

The comparison between the results from the proposed component-level experiments and mathematical modeling confirms the models' ability to accurately represent the dynamic characteristics of each component. The force–displacement graphs corresponding to one cycle of each component show a strong correlation, and relative errors are calculated to quantify model performance. While the axial reaction force of the gasket does not achieve an RMSE within 10% of the maximum reaction force, the reaction force profiles of the other components meet this criterion, indicating that the parameters of the mathematical models are accurately identified, validating the modeling process as a generalized procedure.

The framework's performance is further validated through a parametric study involving the front unbalanced mass, rear unbalanced mass, and phase differences between these masses. Additionally, the transient vibration characteristics observed during RPM changes in the spin cycle are assessed by dividing the RPM profile into eight regions and extracting the RMS values of the vibrations in each region, comparing them with experimental results. Although the error is larger in cases involving phase differences than for a single unbalanced mass, the overall average error is 20.11%, with a standard deviation of 4.10%, demonstrating that the model is generalized for various conditions. Consequently, despite several factors requiring verification for each component, the proposed framework accurately predicts the vibration behavior of a front-loading washing machine.

Acknowledgments

The research reported in this paper has been supported by LG Electronics, Republic of Korea.

Conflicts of Interest

The authors declare no conflicts of interest.

Data Availability Statement

The data that support the findings of this study are available from the corresponding author upon reasonable request.

References

1. W. Schiehlen, "Multibody System Dynamics: Roots and Perspectives," *Multibody System Dynamics* 1 (1997): 149–188.

2. A. A. Shabana, "Flexible Multibody Dynamics: Review of Past and Recent Developments," *Multibody System Dynamics* 1 (1997): 189–222.

3. J. Yang, Q. Wang, Z. Zhang, Z. Liu, S. Xu, and G. Li, "Dynamic Modeling and Analysis of the Looped Space Tether Transportation System Based on ANCF," *International Journal of Mechanical System Dynamics* 2, no. 2 (2022): 204–213.

4. Z. Bai, F. Xu, and J. Zhao, "Numerical and Experimental Study on Dynamics of the Planar Mechanical System Considering Two Revolute Clearance Joints," *International Journal of Mechanical System Dynamics* 1, no. 2 (2021): 256–266.

5. T. Nygårds and V. Berbyuk, "Multibody Modeling and Vibration Dynamics Analysis of Washing Machines," *Multibody System Dynamics* 27 (2012): 197–238.

6. J.-S. Jang, J.-H. Jin, H.-Y. Jung, J.-H. Park, J.-W. Lee, and W.-S. Yoo, "Multibody Dynamic Analysis of a Washing Machine With a Rapid Change of Mass During Dehydration," *International Journal of Precision Engineering and Manufacturing* 17 (2016): 91–97.

7. B. Sánchez-Tabuenca, C. Galé, J. Lladó, C. Albero, and R. Latre, "Washing Machine Dynamic Model to Prevent Tub Collision During Transient State," *Sensors* 20, no. 22 (2020): 6636.

8. J.-S. Jeong, J.-H. Sohn, C.-J. Kim, and J.-H. Park, "Dynamic Analysis of Top-Loader Washing Machine With Unbalance Mass During Dehydration and Its Validation," *Journal of Mechanical Science and Technology* 37, no. 4 (2023): 1675–1684.

9. E. Öztürk, "On the Dynamics of a Washing Machine With Flexible Components," *Noise Control Engineering Journal* 58, no. 6 (2010): 572–590.

10. F. Wagner and F. Pfeiffer, *Dynamics of Washing Machines: Mechanical Model and Simulation* (American Society of Mechanical Engineers, 1999), 351–359.

11. W.-S. Yoo, S.-W. Jung, J.-H. Park, B.-S. Chung, J.-H. Lee, and G.-H. Nho, "Mathematical Model of Transition Velocity-Dependent (TVD) Friction for a Free-Stroke Damper in a Washing Machine," in *International Design Engineering Technical Conferences and Computers and Information in Engineering Conference* (2009), 781–786.

12. T. Funke and D. Bestle, "Physics-Based Model of a Stroke-Dependent Shock Absorber," *Multibody System Dynamics* 30 (2013): 221–232.

13. A. Ulasyar and I. Lazoglu, "Design and Analysis of a New Magneto Rheological Damper for Washing Machine," *Journal of Mechanical Science and Technology* 32 (2018): 1549–1561.

14. S. Kulkarni, U. Dabade, and P. Maskar, "Design and Development of Magneto-Rheological Damper for Vibration Attenuation in Household Washing Machine," *Materials Today: Proceedings* 80 (2023): 1116–1121.

15. M. M. Ferdaus, M. M. Rashid, M. H. Hasan, and M. A. Rahman, "Optimal Design of Magneto-Rheological Damper Comparing Different Configurations by Finite Element Analysis," *Journal of Mechanical Science and Technology* 28 (2014): 3667–3677.

16. M. M. Rashid, M. M. Ferdaus, M. H. Hasan, and A. Rahman, "ANSYS Finite Element Design of an Energy Saving Magneto-Rheological Damper With Improved Dispersion Stability," *Journal of Mechanical Science and Technology* 29 (2015): 2793–2802.

17. D. In, D.-G. Lim, J. Min, et al., "Robust Design Optimization of Spin Algorithm to Reduce Spinning Time and Vibration in Washing Machine," *AIP Advances* 14, no. 3 (2024): 035219.

18. M. A. Bezerra, R. E. Santelli, E. P. Oliveira, L. S. Villar, and L. A. Escaleira, "Response Surface Methodology (RSM) as a Tool for Optimization in Analytical Chemistry," *Talanta* 76, no. 5 (2008): 965–977.

19. R. H. Myers, D. C. Montgomery, and C. M. Anderson-Cook, *Response Surface Methodology: Process and Product Optimization Using Designed Experiments* (John Wiley & Sons, 2016).

20. W. S. Kang, C. K. Choi, and H. H. Yoo, "Stochastic Modeling of Friction Force and Vibration Analysis of a Mechanical System Using the Model," *Journal of Mechanical Science and Technology* 29 (2015): 3645–3652.

21. S. Sharma and F. Kienhöfer, *The Effective Evaluation of Truck Safety for an Alternative Parallel South African PBS Legislation* (University of the Witwatersrand, Faculty of Engineering and the Built ..., 2013).

22. S. V. Shah, P. V. Nandihal, and S. K. Saha, "Recursive Dynamics Simulator (ReDySim): A Multibody Dynamics Solver," *Theoretical and Applied Mechanics Letters* 2, no. 6 (2012): 063011.

23. Y. L. Hwang, J. K. Cheng, and V. T. Truong, "Computer-Aided Dynamic Analysis and Simulation of Multibody Manufacturing Systems," *Applied Mechanics and Materials* 764–765 (2015): 757–761.

24. S. Kim, M. Pak, Y. Kim, and H. Lee, "Motor Noise Source Identification and Tub Vibration Prediction in a Drum Washing Machine," *Applied Acoustics* 210 (2023): 109434.